

**First-Principles Study of Low Miller Index Ni<sub>3</sub>S<sub>2</sub> Surfaces in Hydrotreating Conditions****Yosslen Aray\****Centro de Química, IVIC, Apartado 21827, Caracas 1020 A, Venezuela***David Vega***FACYT, Universidad de Carabobo, Valencia, Venezuela***Jesus Rodriguez***Centro de Química, IVIC, Apartado 21827, Caracas 1020 A, Venezuela***Alba B. Vidal***Centro de Química, IVIC, Apartado 21827, Caracas 1020 A, Venezuela***Maria Elena Grillo***Tyndall National Institute, Lee Maltings, Cork, Ireland***Santiago Coll***Centro de Química, IVIC, Apartado 21827, Caracas 1020 A, Venezuela**Received: August 11, 2008; Revised Manuscript Received: November 7, 2008*

Density functional theory (DFT) calculations combined with surface thermodynamic arguments and the Gibbs–Curie–Wulff equilibrium morphology formalism have been employed to explore the effect of the reaction conditions, temperature ( $T$ ), and gas-phase partial pressures ( $p_{\text{H}_2}$  and  $p_{\text{H}_2\text{S}}$ ) on the stability of nickel sulfide (Ni<sub>3</sub>S<sub>2</sub>) surfaces. Furthermore, the strength and nature of chemical bonds for selected Ni<sub>3</sub>S<sub>2</sub> surface cuts were investigated with the quantum theory of atoms in molecules methodology. A particular analysis of the electrostatic potential within this theoretical framework is performed to study the potential activity of nickel sulfide nanoparticles as hydrodesulfurization (HDS) catalysts. The calculated thermodynamic surface stabilities and the resulting equilibrium morphology model suggest that unsupported Ni<sub>3</sub>S<sub>2</sub> nanoparticles mainly expose (111) and (11̄1) type surface faces in HDS conditions. Analysis of the electrostatic potential mapped onto a selected electron density isocontour (0.001 au) on those expose surface reveals a poor potential reactivity toward electron-donating reagents (i.e., low Lewis acidity). Consequently, a very low attraction between coordinatively unsaturated active sites (Lewis sites) exposed at the catalytic particles and the S atoms coming from reagent polluting molecules does inactive these kinds of particles for HDS.

**Introduction**

Transition metal sulfides (TMS) belong to a very important class of catalysts characterized by being stable under severe sulfo-reductive conditions in hydroprocessing of petroleum-based feedstocks.<sup>1,2</sup> In hydrodesulfurization (HDS) processes, organosulfur molecules are removed from oil by reacting with hydrogen to form H<sub>2</sub>S and hydrocarbons.<sup>1–3</sup> The catalytic process of sulfur removal involves both a C–S bond cleavage and a hydrogenation step. Studies of HDS of dibenzothiophene (DBT) over unsupported sulfides<sup>4</sup> showed that ability of a particular sulfide to catalyze the HDS reaction is related to the position of the TM in the periodic table. A characteristic volcano-type dependence of the activity of the metal as a function of its position in the periodic table for second-row (4d) and third-row (5d) transition metals was found.<sup>4</sup> The first-row (3d) TMS are much less active than sulfides of the second- and third-row metals. A maximum is attained for RuS<sub>2</sub>, OsS<sub>2</sub>,

NiMoS<sub>x</sub> and Rh<sub>2</sub>S<sub>3</sub> while Ni<sub>3</sub>S<sub>2</sub> is among the less active sulfides. In HDS, the sulfide surfaces are reduced by sulfur elimination using a large excess of hydrogen at temperatures ranging from 573 to 673 K, creating coordinatively unsaturated sites (CUS) or vacancies around the metals. CUS behave as electron-withdrawing sites, whose properties may be regarded as a Lewis-type centers interacting with electron-donating organic substrates.<sup>4–6</sup> The nature of these sites is suggested to be intimately related to the metal–sulfur bond strength.<sup>2,4,5,7,8</sup> Fundamental studies support the view that differences in catalytic activity are related to variations in the concentration of CUS (Lewis acid sites), which in turn depend on the metal–sulfur bond strength.<sup>9–21</sup> In this regard, it was found<sup>21</sup> that the experimental HDS<sup>4</sup> activities of the entire TMS series,  $A_{\text{TMS}}$ , fit on a single volcano master curve when plotted against their bulk cohesive energy per metal–sulfur bond. This correlation was corroborated<sup>19</sup> by means of a bond concept rigorously defined in the context of the topological theory of the electronic density,  $\rho(\mathbf{r})$ .

Nickel (and cobalt)-promoted molybdenum sulfide catalysts have for many years been considered to be among the most

\* To whom correspondence should be addressed: e-mail [yaray@ivic.ve](mailto:yaray@ivic.ve); Fax (+58) 212 504 1350.

important catalysts in refinery service. Studies using X-ray absorption fine structure (EXAFS) have established that the active Mo atoms are present as small MoS<sub>2</sub>-like nanostructures.<sup>22,23</sup> Adsorption and activity experiments<sup>24,25</sup> have revealed that the active sites reside at the edges of the MoS<sub>2</sub> structures. Moreover, a recent study, combining high-resolution scanning tunneling microscopy (STM) experiments and density-functional theory (DFT) calculations,<sup>26</sup> has shown that the MoS<sub>2</sub> nanoclusters adopt a hexagonal shape exposing two different types of edges, namely, Mo edges covered with S monomers and fully sulfur-saturated S edges. First-principles surface thermodynamics combined with Gibbs–Curie–Wulff<sup>21,26c,27–30</sup> based morphology modeling have provided a novel way to bridge the gap between the zero-temperature (0 K) DFT results and those obtained under realistic reaction conditions. By means of this methodology, a better understanding of important characteristics of the active phase can be afforded. In doing so, characteristic features of the catalytic nanocrystallites, such as localization and role of the promoter, electronic properties, and equilibrium morphology, can be accounted for. Particularly, effects of morphological changes of the active nanoparticles undergone upon reactions, or induced either by promoter addition or by the support, can now be addressed explicitly.

The “quantum theory of atoms in molecules” (QTAIM) of Bader et al. is very useful to obtain the chemical information from the charge density.<sup>31–40</sup> QTAIM is a firm, rigorous, and quantum mechanically well-defined theory based on observables such as the electron density or energy density fields. QTAIM provides a quantitative link between the total electron density (regardless of how it was generated: calculated or experimental) and important physical properties of a molecule, bypassing the wave function in the analysis. In particular, it provides a rigorous definition of chemical bond and geometrical structure for all types of molecules and solids and has proven to be useful in the analysis of physical properties of insulators, pure metals, and alloys.<sup>34–38</sup> High-quality experimental densities of minerals,<sup>41–45</sup> covalent,<sup>46</sup> metallic,<sup>47</sup> and molecular crystals<sup>48–51</sup> have been analyzed in terms of QTAIM concepts. Furthermore, QTAIM calculations on simple metals,<sup>37,52–54</sup> alloys, and intermetallic phases<sup>55–59</sup> have also been reported as well as on molecular,<sup>54,60–62</sup> covalent, and ionic crystals.<sup>38,45,46,53,63,64</sup> Additionally, the most agreeable feature of QTAIM might be is that it lends itself very well to visualization of the individual atoms in both complex molecular systems and in condensed matter using computer graphics. The connection between the topology of the electron density and the chemical and structural stability of isolated molecules and crystals has been well established.<sup>32,34,36–38,19,65</sup> Recently, the nature of the MoS<sub>2</sub> catalyst edges using QTAIM was studied.<sup>20</sup> Two interesting facts were observed, namely, the S–Mo–S trilayers stacking arrangement is bonded by S–S interlayer bonds similarly to the bulk case, and a much bigger electron density on the graphs describing the Mo edge suggests to be the origin of the well-known easiness to create vacancies on the S edge. Additionally, it has been found that potential active sites on the catalyst surface can be localized by direct visualization of the outermost surface atoms basin. These atoms, similarly to an atom within an isolated molecule, have considerable open parts that extend to infinity. Exposed atoms are open, or unbounded, beyond the surface. A practical atom definition<sup>37</sup> is to cap these atoms with an electron density,  $\rho(\mathbf{r})$ , isocontour with a small value representing the van der Waals envelope of the system. A very efficient way to visualize and quantify the strength of the active sites is to map

the electrostatic potential onto this external density isocontour defining the atomic borders.<sup>20</sup>

The present work is aimed at further improve the understanding of HDS catalysts exploring, in particular, the nature of the active sites of Ni<sub>3</sub>S<sub>2</sub> nanoparticles. The results will be present in three sections: (i) By means of a combination of DFT total energy calculations and classical thermodynamics, the relative stabilities of low Miller index nickel sulfide (Ni<sub>3</sub>S<sub>2</sub>) surfaces under *realistic* HDS conditions of temperature ( $T$ ) and partial pressures of the gas mixture ( $p_{\text{H}_2}$  and  $p_{\text{H}_2\text{S}}$ ) have been studied. Based on the calculated thermodynamic surface stabilities, the equilibrium Gibbs–Curie–Wulff morphology is determined. (ii) The nature of the chemical bonding and structural stability of the most stable surfaces were studied using QTAIM. (iii) The nature of the HDS active sites (Lewis acid sites) was studied using the electrostatic potential within the theoretical framework described in ref 20.

### Thermodynamic Calculations

In industrial working conditions<sup>21,26c,27–30,66–68</sup> involving the presence of H<sub>2</sub> and H<sub>2</sub>S in the gas/liquid phase (reactive atmosphere) in chemical equilibrium with the surface, a variation of the surface coverage should occur according to the reaction



where  $-\square_n$  denotes  $n$  sulfur vacancy by unit cell. The surface stability in this environment can be determined by calculating the surface Gibbs free energy,  $\gamma(T, p_i)$ , at temperature  $T$  and pressure  $p_i$  of the gas phase components. The general thermodynamic formula for  $\gamma(T, p_i)$  is

$$\gamma(T, p_i) = \frac{1}{A} [G - \sum_i N_i \mu_i(T, p_i)] \quad (2)$$

where  $G$  is the Gibbs free energy of the solid with a surface of area  $A$ . The solid surface is modeled by a piece of material (slab) in a grand canonical ensemble at constant temperature ( $T$ ) and total pressure ( $P$ ). The material slab is infinite (periodic) within the surface plane with a vacuum of 1 nm separating it from its next periodically repeated image parallel to the surface.  $\mu_i(T, p_i)$  is the chemical potential of the various species  $i$  present in the system, and  $N_i$  gives the number of atoms of the  $i$ th component contained in the solid slab model. For the Ni<sub>3</sub>S<sub>2</sub> surfaces, eq 2 is

$$\gamma(T, p) = \frac{1}{A} [E_{\text{Ni}_3\text{S}_2}^{\text{surface}} - N_{\text{Ni}} \mu_{\text{Ni}}(T, p) - N_{\text{S}} \mu_{\text{S}}(T, p)] \quad (3)$$

where  $\mu_{\text{Ni}}$  and  $\mu_{\text{S}}$  are the chemical potentials of a Ni atom and an S atom, respectively, and  $\gamma(T, p)$  is normalized to energy per unit area by dividing through the surface area  $A$ . Here the total Gibbs free energy of the content of slab ( $G$ ) is approximated by the ab initio electronic energy  $E_{\text{Ni}_3\text{S}_2}^{\text{surface}}$  calculated at zero temperature and pressure. Neglecting the temperature dependence of  $G$  implies that vibrations of the atoms in the solid are not taken into account in the calculations. Therefore, the temperature dependence of the surface energy  $\gamma(T, p)$  is introduced by the dominant dependence of the chemical potentials of the gas-phase mixture (H<sub>2</sub> + H<sub>2</sub>S) in equilibrium with the surface. The zero-temperature electronic energy approximation

to  $G$  of the material slab used in a number of previous studies of this type has already given reasonably accurate results.<sup>20,21,24</sup>

At equilibrium,  $\mu_S$  is the same in all the phases that are in contact and contain sulfur. At equilibrium between the bulk  $\text{Ni}_3\text{S}_2$  and its components, the following relationships are satisfied:

$$3\mu_{\text{Ni}} + 2\mu_S = \mu_{\text{Ni}_3\text{S}_2}(\text{bulk})$$

Taking the ab initio zero-temperature total energy ( $E_{\text{Ni}_3\text{S}_2}(\text{bulk})$ ) for the chemical potential of the bulk phase

$$3\mu_{\text{Ni}} + 2\mu_S = E_{\text{Ni}_3\text{S}_2}(\text{bulk})$$

As the equilibrium condition is assumed, the chemical potential of Ni in the surface energy expression  $\gamma(T,p)$  is equal to the respective chemical potential of Ni in the bulk phase

$$\mu_{\text{Ni}} = \frac{1}{3}E_{\text{Ni}_3\text{S}_2}(\text{bulk}) - \frac{2}{3}\mu_S \quad (4)$$

Combining then eqs 3 and 4, the temperature dependence of the surface Gibbs free energy enters only through the chemical potentials of the gases in contact with the surface  $\mu_S = \mu_{\text{H}_2\text{S}} - \mu_{\text{H}_2}$

$$\gamma(T,p) = \frac{1}{2A} \left[ E_{\text{Ni}_3\text{S}_2}^{\text{surface}} - \frac{N_{\text{Ni}}}{3}E_{\text{Ni}_3\text{S}_2}(\text{bulk}) + \left( \frac{2}{3}N_{\text{Ni}} - N_S \right)\mu_S(T,p) \right] \quad (5)$$

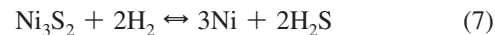
In practical calculations, the chemical potentials of the gas-phase mixture ( $\text{H}_2 + \text{H}_2\text{S}$ ) are evaluated using the general thermodynamic formula assuming ideal gas behavior

$$\mu_S = \mu_{\text{H}_2\text{S}} - \mu_{\text{H}_2}$$

$$\mu_S(T) = \Delta E_{\text{el}} + \Delta ZPE + \Delta H(T) - T\Delta S(T) + RT \ln \left( \frac{p_{\text{H}_2\text{S}}}{p_{\text{H}_2}} \right) \quad (6)$$

Here,  $\Delta H(T)$  and  $\Delta S(T)$  stand for enthalpy and entropy differences, respectively, at  $T$  for  $\text{H}_2\text{S}$  and  $\text{H}_2$ , and  $\Delta E_{\text{el}}$  stands for the difference of their internal energies ( $E_{\text{el}}(\text{H}_2\text{S}) - E_{\text{el}}(\text{H}_2)$ ), which are approximated by their zero-temperature DFT total energies.  $\Delta ZPE$  represents the zero-point vibrational energy term [ $H_{\text{H}_2\text{S}}(0) - E_{\text{el}}(\text{H}_2\text{S})$ ] – [ $H_{\text{H}_2}(0) - E_{\text{el}}(\text{H}_2)$ ] calculated through evaluation of the Hessian matrix elements using the normal modes analysis module implemented in the program DMol<sup>3</sup>.<sup>85,86</sup>

Large values of  $\mu_S$  correspond to sulfur-rich conditions, whereas small values of  $\mu_S$  relate to strongly reducing conditions, in which hydrogen is more abundant than  $\text{H}_2\text{S}$  in the gas phase. The chemical potential of sulfur,  $\mu_S$ , cannot take arbitrarily large values but is determined by the chemical equilibrium between the surface and the gas phase. Therefore, it is necessary to determine the effect of the experimental conditions,  $T$  and gas-mixture partial pressures, upon the chemical potential of sulfur. The reduction of bulk  $\text{Ni}_3\text{S}_2$  into metallic nickel can be considered as the limit for decreasing the sulfur chemical potential



This limit can be evaluated by the calculation of the Gibbs free energy of reaction according to the following equation:

$$\Delta_f G = 3\mu_{\text{Ni}}(\text{bulk}) - \mu_{\text{Ni}_3\text{S}_2}(\text{bulk}) + 2\mu_S = 3E_{\text{Ni}}(\text{bulk}) - 3E_{\text{Ni}_3\text{S}_2}(\text{bulk}) + 2\mu_S \quad (8)$$

where the DFT total energies,  $E_{\text{Ni}}(\text{bulk})$  and  $E_{\text{Ni}_3\text{S}_2}(\text{bulk})$ , calculated using DMol<sup>3</sup> for trigonal  $\text{Ni}_3\text{S}_2$  (space group R32(155)) and for bulk nickel in a face cubic center (fcc) crystal structure have been used to approximate their chemical potentials,  $\mu_{\text{Ni}_3\text{S}_2}$  and  $\mu_{\text{Ni}}$ . Hence,  $\mu_S > \frac{1}{2}[E_{\text{Ni}_3\text{S}_2}(\text{bulk}) - 3E_{\text{Ni}}(\text{bulk})] > -4.29$  eV.

It appears that reduction should occur if  $\mu_S$  is lower than -4.29 eV (i.e.,  $p(\text{H}_2\text{S})/p(\text{H}_2) < 10^{-5}$ ). Therefore,  $\text{Ni}_3\text{S}_2$  is not stable for a  $\text{H}_2\text{S}/\text{H}_2$  ratio lower than  $10^{-5}$ , at which metallic nickel would condense at the surface. In the regime of high sulfur chemical potentials, the  $p(\text{H}_2\text{S})/p(\text{H}_2)$  ratio is constrained by the equilibrium



As for the low chemical potential threshold, the numerical value of the upper limit has been deduced from the calculation of the Gibbs free energy of reaction

$$\Delta_f G = \mu_{\text{S}_\alpha}(\text{bulk}) - \mu_S = E_{\text{S}_\alpha}(\text{bulk}) - \mu_S \quad (10)$$

where  $E_{\text{S}_\alpha}(\text{bulk})$  is the DFT total energy calculated with DMol<sup>3</sup> for the crystalline  $\alpha$ -orthorhombic structure of sulfur with 128 atoms per unit cell. Thus, the maximum threshold is calculated to be  $\mu_S < E_{\text{S}_\alpha}(\text{bulk}) < -3.08$  eV. It appears that reaction 7 becomes possible if  $\mu_S$  is greater than -3.08 eV ( $p(\text{H}_2\text{S})/p(\text{H}_2) > 10^4$ ). Thus, the variation range for  $\mu_S$  (in eV) should be  $-4.29 < \mu_S < -3.08$ , leading to a partial pressure range of  $10^{-5} < p(\text{H}_2\text{S})/p(\text{H}_2) < 10^4$  for the gas mixture.

### The QTAIM Theory

The topological properties of a crystal charge distribution are summarized by its critical points (CP).<sup>31–40</sup> These are points where the gradient vector field,  $\nabla\rho(\mathbf{r})$ , vanishes, and they are classified by the  $\rho(\mathbf{r})$  curvatures or three eigenvalues  $\lambda_i$  ( $i = 1, 2$ , and 3) of the Hessian matrix ( $H_{ij} = \partial^2\rho(\mathbf{r})/\partial x_i \partial x_j$ ). They are labeled by their rank (number of nonzero eigenvalues) and signatures (excess number of positive over negative eigenvalues) and correspond to maxima (3, -3), minima (3, +3), and saddle points (3, +1) and (3, -1). Every CP has a characteristic pattern of trajectories or gradient paths of  $\rho(\mathbf{r})$ . The trajectories originate and end at critical points. Only the (3, -3) points are three-dimensional trajectory attractors: trajectories only terminate at this CP. The (3, -3) points occur generally at the nuclear positions so that each nucleus is a three-dimensional point attractor in the vector field  $\nabla\rho(\mathbf{r})$ . The region traversed by the gradient paths, which terminate at a given attractor, defines the basin of the attractor. A (3, -1) CP, the bond critical point (b), is found between every pair of neighboring nuclei. It represents both local maxima in two directions and a local minimum in the third direction. The gradient paths associated with the negative eigenvalues at the (3, -1) point terminate at this CP and define the interatomic surfaces (IAS) that partition the

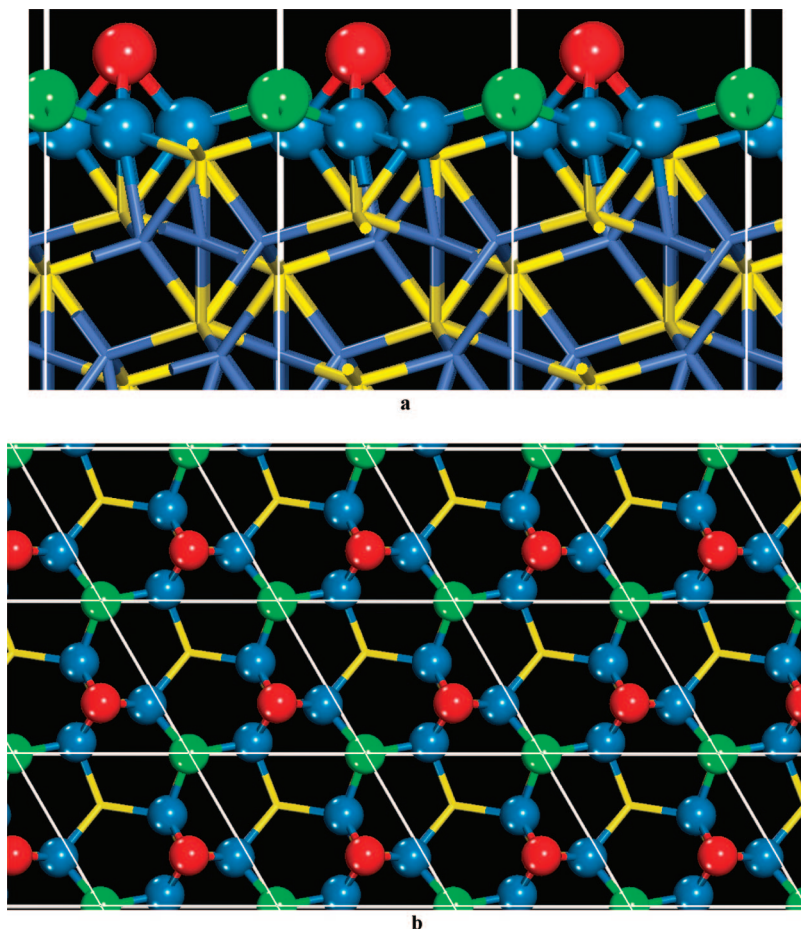


**Figure 1.** (a) Side view and (b) top view of a ball and cylinders model of the Ni<sub>3</sub>S<sub>2</sub> (111\_S2) surface. Several unit cells (white lines) are shown. Red and green spheres denote the outermost sulfur atoms. Light blue spheres denote the outermost nickel atoms. Yellow and blue cylinders denote the internal S and Ni atoms, respectively. Systematic removal of, first, one red sulfur atom by unit cell and then a green one produces the (111\_S1) and (111\_S0) surfaces, respectively.

crystal into unique fragments (the atomic basins). In general, the interatomic boundaries of atoms within a crystal are at the interception of their interatomic surfaces. The unique pair of trajectories associated with the positive eigenvalue of the (3, -1) CP originates at this point and terminate at the neighboring attractors. These two unique gradient paths define a line (the bond path) linking the nuclei (n), along which the charge density is a maximum with respect to any neighboring line. The network of bond paths defines a graph, namely the crystal graph, which describes the atomic connectivity and structure within a crystal cell. The other CPs occur as a consequence of the geometrical arrangements of bond paths, and they define the remaining elements of crystal structure, namely rings and cages. If the bond paths are linked to form a ring of bonded atoms, then a (3, +1) CP is found in the interior of the ring. The eigenvectors associated with the two positive eigenvalues of the (3, +1), a ring (r) CP, generate an infinite set of gradient paths which originate at the CP and define a surface, called the ring surface. All of these trajectories terminate at the ring nuclei or at the bond CPs whose bond paths form the perimeter of the ring. The single negative eigenvector of the ring CP generates a pair of gradient paths, which terminate at the CP and define a unique axis perpendicular to the ring surface at the critical point. The (3, +3) or cage (c) CPs are located inside a cage nuclear arrangement. The charge density is a local minimum at a cage CP and in crystals; it is the main source of trajectories of  $\nabla\rho(\mathbf{r})$ : trajectories only originate at such CPs and terminate at nuclei,

bond, or ring CPs. The type and numbers of CPs for an extended system<sup>34,39</sup> satisfy the Morse invariant relationships

$$n - b + r - c = 0 \quad (11)$$

### The Electrostatic Potential Methodology

The nature of active sites can be particularly explored using the electrostatic potential,  $V(\mathbf{r})$ , which lets us directly determine where the electron-rich sites in a molecule or crystal are localized.<sup>69–79</sup>  $V(\mathbf{r})$  at a point  $\mathbf{r}$  generated by a molecule or crystal is given by

$$V(\mathbf{r}) = V_N(\mathbf{r}) + V_E(\mathbf{r}) \quad (12)$$

where the two terms  $V_N(\mathbf{r})$  and  $V_E(\mathbf{r})$  represent the bare nuclear and electronic contributions, respectively, to the total electrostatic potential. The sign of  $V(\mathbf{r})$  at a given point indicates whether the nuclear (positive) or electronic (negative) effects are dominant. The electrostatic potential at  $\mathbf{r}$  generated by the total charge distribution,  $\rho^{\text{tot}}$ , of a periodic system is given by

$$V(\mathbf{r}) = \sum_n \int \rho^{\text{tot}}(\mathbf{r}' - \mathbf{R}_n) |\mathbf{r} - \mathbf{r}'|^{-1} d\mathbf{r}' \quad (13)$$

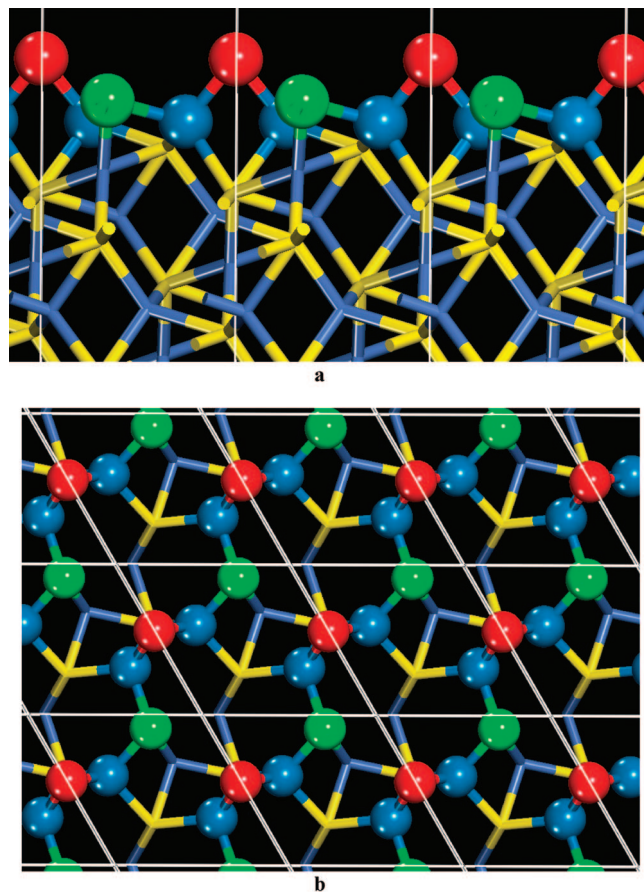


**Figure 2.** (a) Side view and (b) top view of a ball and cylinders model of the  $\text{Ni}_3\text{S}_2$  (111-S2) surface. Several unit cells (white lines) are shown. Red and green spheres denote the outermost sulfur atoms. Light blue spheres denote the outermost nickel atoms. Yellow and blue cylinders denote the internal S and Ni atoms, respectively. Removal of one red sulfur atom by unit cell produces the (111-S1) surface.

The summation extends to all direct lattice vectors, the prime on the integral sign indicating that an infinitesimal region about  $\mathbf{r} = \mathbf{r}'$  is excluded from the domain of integration to avoid divergent nuclear self-interactions terms that would otherwise arise in the electrostatic energy per cell.  $\rho^{\text{tot}}$  may be decomposed into electronic and nuclear components

$$\rho^{\text{nuc}}(\mathbf{r}) = \sum_a q_a \delta(\mathbf{r}_a, \mathbf{r}) \quad (14)$$

where the summation extends to all the reference cell nuclei, with atomic numbers and position vectors denoted  $q_a$  and  $\mathbf{r}_a$ , respectively.

$$\rho^{\text{el}}(\mathbf{r}) = - \sum_{ij} \sum_{\mu\nu} \mathbf{P}_{\mu\mathbf{R}_i\nu\mathbf{R}_j} \chi_\mu(\mathbf{r} - \mathbf{R}_i) \chi_\nu^*(\mathbf{r} - \mathbf{R}_j) \quad (15)$$

where  $\mathbf{P}$  is the density matrix and  $\chi_\mu(\mathbf{r} - \mathbf{R}_i)$  is the  $\mu_{th}$  reference cell basis function translated by the direct lattice vector  $\mathbf{R}_i$ . The summations over  $i$  and  $j$  extend to all direct lattice vectors, while those over  $\mu$  and  $\nu$  include all the basis functions of the reference cell. Substitution of eq 15 and eq 14 into eq 13 gives the nuclear and electronic  $V(\mathbf{r})$  contributions.

For the region nearest to the nucleus  $V_N$  dominates, and  $V(\mathbf{r})$  has similar topology to the electron density,<sup>80,81</sup>  $\rho(\mathbf{r})$ , i.e., positive-valued maxima at the nuclear site and a positive-valued

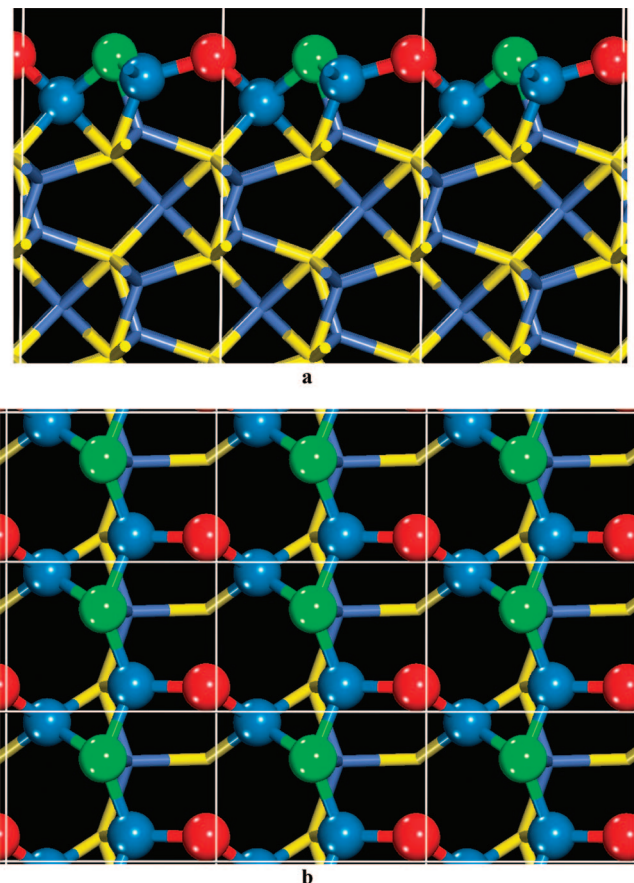


**Figure 3.** (a) Side view and (b) top view of a ball and cylinders model of the  $\text{Ni}_3\text{S}_2$  (110-S2) surface. Several unit cells (white lines) are shown. Red and green spheres denote the outermost sulfur atoms. Light blue spheres denote the outermost nickel atoms. Yellow and blue cylinders denote the internal S and Ni atoms, respectively.

saddle point between every pair of bonded atoms. Nevertheless, the existence of maxima is ruled out via an established result that, barring the nuclear position, there cannot exist any strict local maxima in the  $V(\mathbf{r})$  map.<sup>72,73</sup> For the region where  $V_E$  dominates ( $V(\mathbf{r})$  is negative) the  $V(\mathbf{r})$  topography can be more complex. However, it is well-known that lone pairs of electrons as well as double  $\pi$  bonds ( $\text{C}=\text{C}$ ,  $\text{C}=\text{N}$ , etc.) are generally characterized as negative-valued minima.<sup>71,74</sup> In summary, the region nearest to the nucleus is always positive-valued while the region where the potential is negative-valued contains the minima that characterize the atom lone pairs. The minima of the negative region denote the zones to which an approaching electrophile may be attracted. On the contrary, the positive regions do not have maxima that might indicate sites for nucleophilic attack. Nevertheless, Politzer and Sjoberg have shown that by computing  $V(\mathbf{r})$  on the 0.002 electron/bohr<sup>3</sup> contour isosurface<sup>82</sup> of the molecular electronic density  $\rho(\mathbf{r})$ , we can quantify the susceptibility of molecules to nucleophilic attack. They demonstrated that relative magnitudes of the positive electrostatic potential in various regions on this surface do reveal the sites most susceptible to nucleophilic attack. This contour isosurface for a group of diatomic molecules and for methane encompasses at least 95% of the electronic charge and yields physically reasonable molecular dimensions.<sup>82</sup> Mapping on this isosurface, the  $V(\mathbf{r})$  values onto colors let us to identify the host sites in which nucleophiles (most positive zone) and electrophiles (most negative zone) should bind. Additionally, the active sites susceptibility can be quantified determining the minimum and maximum  $V(\mathbf{r})$  values at the determined host

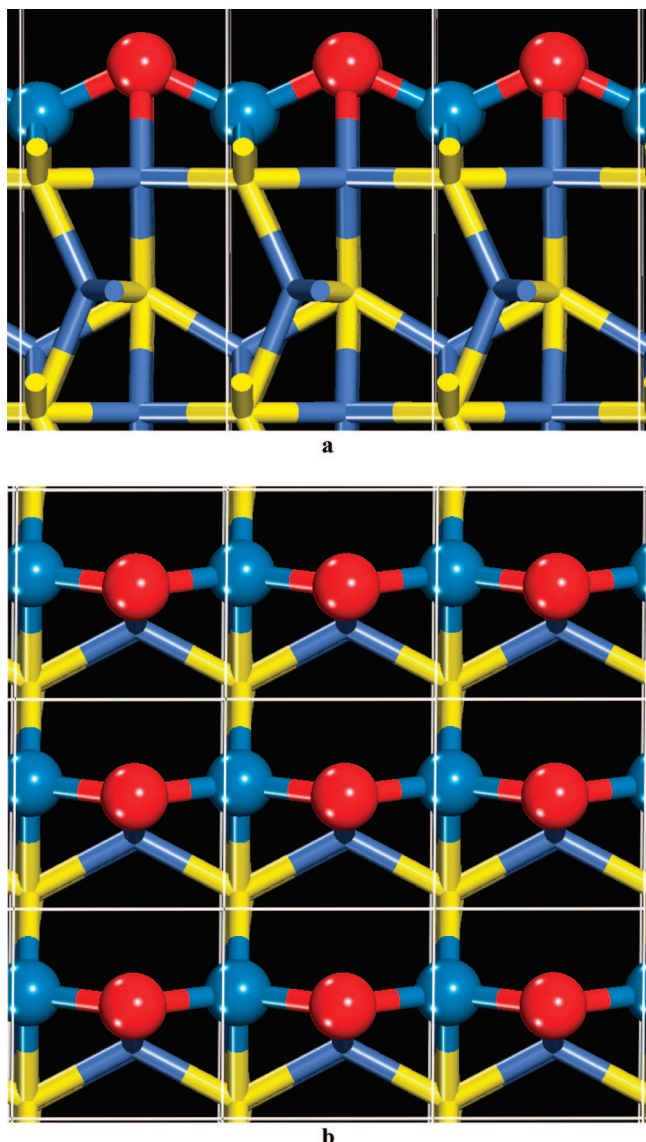


**Figure 4.** (a) Side view and (b) top view of a ball and cylinders model of the Ni<sub>3</sub>S<sub>2</sub> (100\_S1) surface. Several unit cells (white lines) are shown. Red spheres denote the outermost sulfur atoms. Light blue spheres denote the outermost nickel atoms. Yellow and blue cylinders denote the internal S and Ni atoms.

zones using a Newton–Raphson technique like those that we have previously reported for the study of the electronic density<sup>20,83</sup> and electrostatic potential topology.<sup>78,79,84</sup>

### Computational Methodology

$\rho(\mathbf{r})$  and  $V(\mathbf{r})$  were calculated by means of the Dmol<sup>3</sup><sup>85,86</sup> program using the Kohn–Sham Hamiltonian with the gradient-corrected Perdew–Becke–Ernzerhof (PBE) exchange-correlation functional.<sup>87</sup> Dmol<sup>3</sup> calculates variational self-consistent solutions to the DFT equations, expressing numerically the atomic orbital basis functions in an accurate spherical-polar mesh. The solutions to these equations provide the molecular electron densities, which can be used to evaluate the total electrostatic potential of the system. The numerical double- $\zeta$  plus polarization basis set DNP<sup>85,86</sup> was used in all calculations. DMol<sup>3</sup> uses DFT to obtain high accuracy while keeping the computational cost fairly low for an ab initio method. The topology of  $\rho(\mathbf{r})$  was determined using a reported implementation<sup>83</sup> of the Newton–Raphson and fifth-order Cash–Karp Runge–Kutta methods in a  $\rho(\mathbf{r})$  three-dimensional grid.

### Results and Discussion

**Thermodynamic Study.** High-resolution electron microscopy (HREM) and energy dispersive X-ray (EDX) studies have shown the presence of large nickel sulfide particles (up to 50 nm) supported on graphitized carbon or located on the outside of the zeolites pores.<sup>88</sup> In general, the activity of these particles depends on the nature of the exposed faces.<sup>89,90</sup> Ni<sub>3</sub>S<sub>2</sub> bulk is a trigonal type crystal<sup>91</sup> whose lattice is described by the space group R32 (155) with cube edge length  $a = 4.072 \text{ \AA}$ . Its trigonal cell is slightly distorted from a cube; the S atoms form a distorted body-centered cubic array with the Ni atoms located in the center of the distorted tetrahedral holes (three formula units per cell). For this crystal, six types of lowest Miller index surfaces can be formed: (100), (110), (11̄0), (101), (111), and (11̄1). The (111) surface is described by a hexagonal unit cell ( $a = b = 5.76 \text{ \AA}$ ) that contains three outermost Ni atoms (blue spheres in Figure 1) per layer (Ni three-layer) and two S atoms (red and green spheres in Figure 1) above the Ni planes. The S atoms form two layers with different heights on each side of a Ni layer. Each outermost S atom is coordinated to three outermost Ni atoms. Each of the Ni atoms within the three-layer form a trigonal-bipyramidal capped by an outermost S atom (red spheres).

The (11̄1) surface is also described by a hexagonal unit cell (see Figure 2) similar to the (111) one and contains two layers of S atoms (red and green spheres) above the outermost layer of Ni atoms. However, the outermost Ni layer only contains two atoms (blue spheres) by cell, and the outermost S atoms (red spheres) are two coordinated bridging the outermost Ni atoms. The unit cell of the (110) surface (see Figure 3) is a rectangle ( $a = 4.08 \text{ \AA}$ ,  $b = 5.75 \text{ \AA}$ ) that exposes a layer of S atoms containing two nonequivalent atoms (red and green spheres) above the outermost Ni atoms. This outermost Ni layer also exposes two atoms by cell. The (100) surface is described by a square cell (Figure 4) with cell parameter  $a = 3.83 \text{ \AA}$ . This surface exposes a layer of S atoms (red spheres) above the outermost layer of Ni atoms, just one Ni and one S atom by cell. Each outermost Ni atom is coordinated to four S atoms, two on the outermost and two on the second layer of S atoms. The all above surfaces exhibit four-coordinated outermost Ni atoms representing the maximum sulfur coverage for these Ni atoms.

According to eq 1, reduction with H<sub>2</sub> removes outermost S layers, creating sulfur vacancies and decreasing the surface sulfur coverage. For each kind of surface, we have studied the removal of the outermost S atoms until exposing Ni atoms at the surface. The outermost Ni sites will be referred to according to the number of removed sulfur atoms upon reduction, for example, for the (111) surface there will be (111\_S2), (111\_S1), and (111\_S0), respectively. We have modeled these surfaces using periodic slabs of several Ni layers thick (at least seven, the half of the diameter of a typical sulfide particle)<sup>92</sup> with atoms initially located at their ab initio bulk positions. Vacuum layers thicker than 15 Å were used to ensure that there were no interactions between adjacent slabs. The geometry of those models was optimized using algorithms included in the Dmol<sup>3</sup> program.<sup>85</sup> For the (111), (110), and (11̄1) surfaces, 13, 12, and 25 special  $k$ -points generated with a [551], [641], and [771] mesh, respectively, along the three cell axes and the Monkhorst–Pack scheme<sup>85,86</sup> were used to ensure the quality of the results.

In order to study the stability of these surfaces at HDS conditions, their surface Gibbs free energy was calculated using eqs 5 and 6. A typical HDS condition for NiMoS, a very reactive catalysts, is 5% of H<sub>2</sub>S ( $p(\text{H}_2\text{S})/p(\text{H}_2) = 0.05$ ) and  $T = 650 \text{ K}$ .

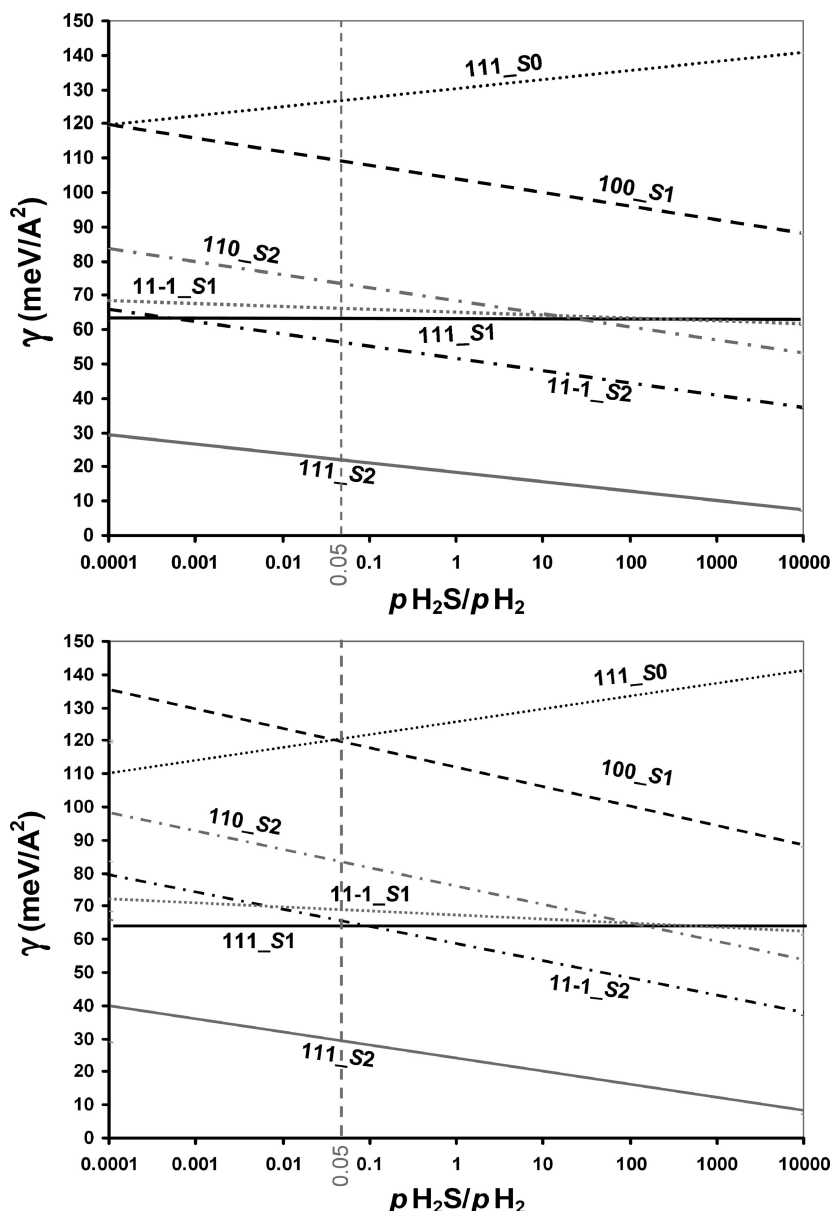


**Figure 5.** Variation of the surface free energy,  $\gamma(T, p(\text{H}_2\text{S})/p(\text{H}_2))$ , as a functions of the  $p(\text{H}_2\text{S})/p(\text{H}_2)$  ratio at 450 K (top) and 650 K (bottom), respectively, for the studied  $\text{Ni}_3\text{S}_2$  surfaces. Each line is labeled by the corresponding sulfur coverage. The gas mixture pressure range of  $10^{-5} < p(\text{H}_2\text{S})/p(\text{H}_2) < 10^4$ , at which  $\text{Ni}_3\text{S}_2$  is stable, is used in the plot.

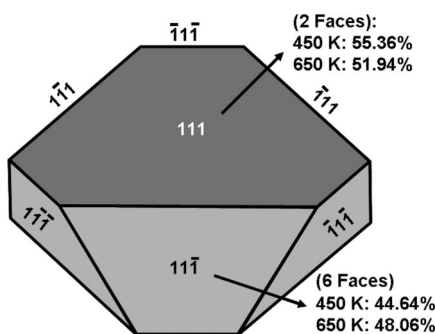


**Figure 6.** Equilibrium Gibbs-Curie-Wulff morphology at HDS conditions of the  $\text{Ni}_3\text{S}_2$  nanoparticles. These particles expose two distorted basal hexagonal ( $111$ ) faces and six ( $11\bar{1}$ )-type faces with trapezium form at the edges.

$\text{H}_2\text{S}$  is mainly product of the desulfurization reactions. Therefore, for less reactive catalysts than  $\text{NiMoS}$ , a more  $\text{H}_2$ -rich environment should be waited and  $p(\text{H}_2\text{S})/p(\text{H}_2)$  should be less than 0.05. To explore the temperature effect, the  $\gamma(T, p(\text{H}_2\text{S})/p(\text{H}_2))$

were determined in a  $T$  range of 400–800 K. In Figure 5 plots of  $\gamma(T, p(\text{H}_2\text{S})/p(\text{H}_2))$  as a function of the  $p(\text{H}_2\text{S})/p(\text{H}_2)$  ratios at 450 and 650 K, respectively, are presented for selected surfaces. In both cases, the  $111_{\text{S}2}$  surface is the most stable for all the  $p(\text{H}_2\text{S})/p(\text{H}_2)$  ratios. The  $(11\bar{1}_{\text{S}2})$ ,  $(110_{\text{S}2})$ , and  $(100_{\text{S}1})$  surfaces are about 34.0, 52.0, and 88.0 meV/ $\text{\AA}^2$ , respectively, less stable with respect to the most stable one over the entire range of calculated pressures at both temperatures. Hence, about the same negative slopes for the surface energy with  $\text{H}_2\text{S}$  pressure (left to right in Figure 5) or the same positive slopes with  $\text{H}_2$  pressure (right to left in Figure 5) were calculated for these surfaces. This indicates that the stability (or instability) of the surfaces increases in the same proportion as the  $\text{H}_2\text{S}$  (or  $\text{H}_2$ ) pressure increases. In contrast, the destabilization energy necessary to create the  $111_{\text{S}1}$  surface from the  $111_{\text{S}2}$  one increases as the  $\text{H}_2\text{S}$  pressure increases.

For all calculated S2 terminations and for the S1-terminated (100) surface, a temperature increase facilitates reduction, as seen in Figure 5. The positive slope of the energy vs  $p_{\text{H}_2}$  brings

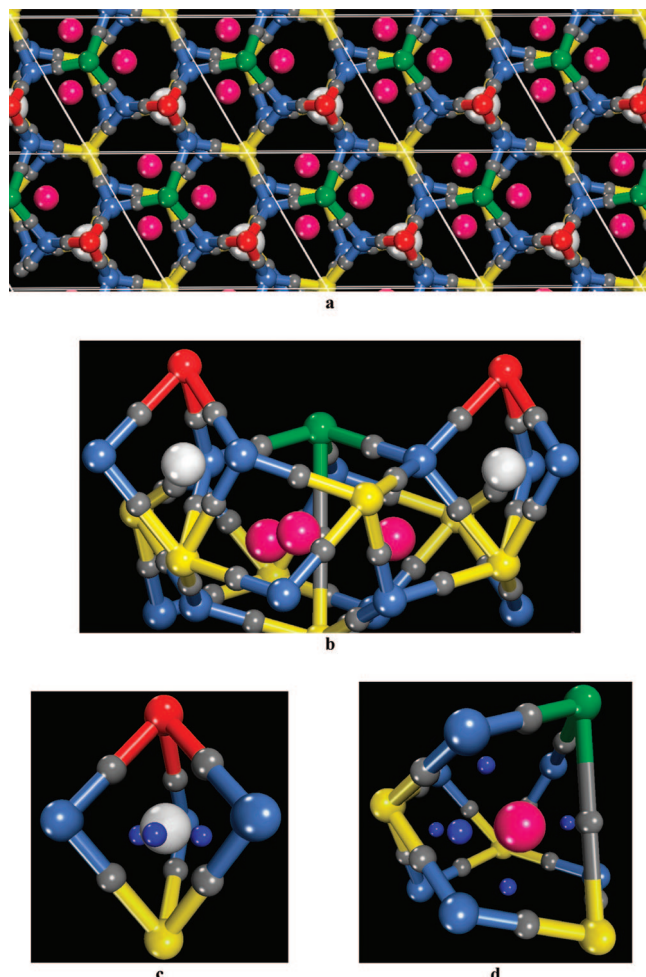


**Figure 7.** (a) Top and (b) side views of the packing polyhedra defined by the critical points of  $\rho(\mathbf{r})$  for the (111-S2) surface. Red and green spheres denote the outermost S atoms located at the first and second sulfur layers, respectively. Light blue spheres denote the outermost Ni atoms. Small gray spheres denote the bond critical points while big white, pink, and orange spheres denote the cage critical points. (c) Side view of the {5, 6, 3} polyhedra defined by the white cage. (d) Side view of the {10, 13, 5} polyhedra defined by the pink cages. Small dark blue spheres in (c) and (d) denote the ring critical points.

the energy of the (111)<sub>S2</sub> surface termination above that of the (111)<sub>S1</sub> surface at 650 K. Hence, upon a temperature increase of 200 K, this surface would be reduced and the (111)<sub>S1</sub> surface would appear at a pressure ratio relatively close to 1% of H<sub>2</sub>S ( $p_{\text{H}_2\text{S}}/p_{\text{H}_2} = 0.01$ ). The negative slope of the energy vs  $p_{\text{H}_2}$  for the completely reduced (111)<sub>S0</sub> surface, in contrast, brings its energy down with increasing  $T$ . At 650 K, the calculated energy,  $\gamma$ , for the reduced (111) is lower than that of the S1-terminated (100) face from H<sub>2</sub> pressures typical for NiMoS HDS catalysis onward. In general, though, the reduced surface terminations are rather thermodynamically unstable (i.e., with associated positive surface energy values) at the relevant temperatures for HDS catalysis. Therefore, from a thermodynamic point of view, it would be rather unlikely to create vacancies (i.e., to activate) by surface sulfur atoms removal out of these surfaces. We have found the same behavior in the entire temperature range studied.

The calculation of the above surface energies makes it possible to deduce the Gibbs–Curie–Wulff<sup>21,26c,27–30</sup> (GCW) equilibrium morphology of the Ni<sub>3</sub>S<sub>2</sub> nanocrystallites. This law connects surface energies and particle morphology. The GCW law states that the distance of a surface plane from the center-

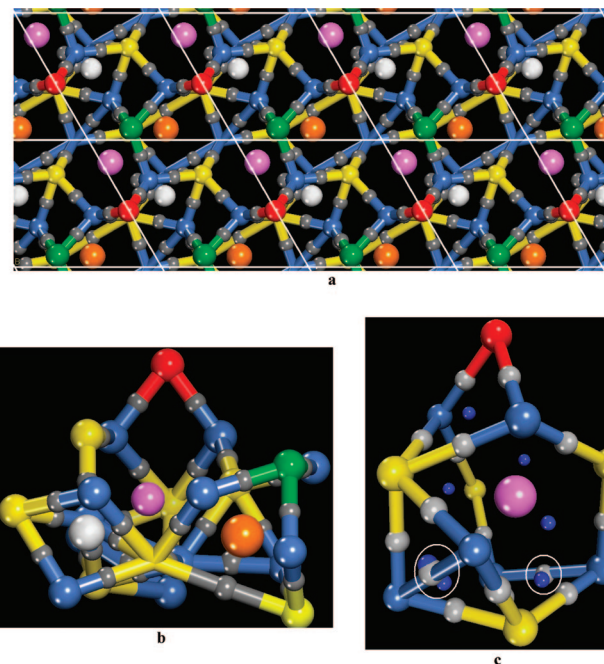


**Figure 8.** (a) Top and (b) side views of the packing polyhedra defined by the critical points of  $\rho(\mathbf{r})$  for the (111-S2) surface. Red and green spheres denote the outermost S atoms located at the first and second sulfur layers, respectively. Light blue spheres denote the outermost Ni atoms. Small gray spheres denote the bond critical points while big white, pink, and orange spheres denote the cage critical points. (c) Side view of the outermost (11, 16, 7) polyhedra defined by the pink cage. Small dark blue spheres in (c) denote the ring critical points. White circles highlight the unstable (very close) ring and bond critical points at the Ni–Ni bond. These critical points coalesce and destroy the faces at the bottom of the polyhedra.

of-mass of the particle,  $d_{hkl}$ , is proportional to the surface energy,  $\sigma_{hkl}$ , of that plane

$$\frac{\sigma_{1(hkl)}}{d_{1(hkl)}} = \frac{\sigma_{2(hkl)}}{d_{2(hkl)}} = \dots = \frac{\sigma_{i(hkl)}}{d_{i(hkl)}} = \text{const} \quad (16)$$

This method has been successfully used to describe the shape of a variety of nanoscale particles.<sup>27–30</sup> Figure 6 shows the ideal equilibrium morphology for a Ni<sub>3</sub>S<sub>2</sub> particle at 450 and 650 K for a  $p_{\text{H}_2\text{S}}/p_{\text{H}_2}$  ratio of 0.05. The particle is an octahedron that exposes two hexagonal (111) faces skirted by six (111)-type faces with trapezium form. At 450 K, the hexagonal and trapezoidal faces occupy 55.36% (27.68 each one) and 44.64% (7.44 each one) of the exposed particle surface, respectively. At 650 K, the hexagonal and trapezoidal faces occupy 51.94 and 48.06%, respectively. For  $p_{\text{H}_2\text{S}}/p_{\text{H}_2} = 0.001$ , the respective areas are 48.30 and 51.70, respectively.

In agreement with the calculated similar slopes of the surface energy ( $\gamma$ ) lines vs  $p_{\text{H}_2\text{S}}/p_{\text{H}_2}$  for the exposed surface faces, their relative percentage contributions to the total particle surface area do not change significantly with the gas mixture pressure ratios at the considered  $T$  range. In summary, the morphologic and DFT studies suggest that nonsupported Ni<sub>3</sub>S<sub>2</sub> nanoparticles would mainly expose surface cuts corresponding to the Miller indexes (111) and (111), with 111-S2 and 111-S2 sulfur coverage, respectively.

**Electron Density Topology Study.** To study the nature of the chemical bonds of the most stable surfaces, we have determined the bond critical points (CP) of the outermost Ni–S bonds. All off the CP per unit cell have been located. Table 1

**TABLE 1: Values of  $\rho(r)$  at the Bond Critical Points,  $\rho_b$ , Equilibrium Bond Length,  $r_e$ , Bonded Radius and Net Atomic Charges for the Studied Models of the (111\_S2) and (111̄\_S2) Nickel Sulfide Surfaces<sup>a</sup>**

(111_S2)						
bond <sup>b</sup>	$\rho_b$	$r_e$	$r_{Ni}$	$r_s$	$Q_s$	$Q_{Ni}$
Ni4–S3 first layer (red)	0.091	2.191	1.026	1.165	-0.382	0.460
Ni4–S3 second layer (green)	0.085	2.228	1.039	1.189	-0.445	0.460
$Ni_3S_2$ bulk <sup>c</sup>	0.076	2.260	1.051	1.209	-0.670	0.447
Ni4–S6 third layer (yellow)	0.070	2.319	1.074	1.245	-0.611	0.460
Ni4–S6 fourth layer	0.066	2.326	1.086	1.240	-0.578	0.460
(111̄_S2)						
bond <sup>b</sup>	$\rho_b$	$r_e$	$r_{Ni}$	$r_s$	$Q_s$	$Q_{Ni}$
Ni4–S2 first layer (red)	0.103	2.130	1.007	1.124	-0.300	0.356
Ni4–S3 second layer (green)	0.097	2.167	1.024	1.143	-0.365	0.356

<sup>a</sup> The number at the right of each atom symbol denotes its coordination number. <sup>b</sup> S3 first layer mean a three-coordinated atom locate at the first layer of sulfur atoms. Colors identify in Figures 1 and 2 the sulfur atoms on the corresponding layers. <sup>c</sup> See ref 93.

reports the determined  $\rho(r)$  values at the bond critical points,  $\rho_b$ , the distance from its nucleus to the associated bond critical point,  $r_s$  and  $r_{Ni}$  (the bonded radius), and the integrated charges of the atoms forming the Ni–S bonds. Figure 7 illustrates the critical points defining the atomic structure for the (111\_S2) surface. The bond paths are shown as cylinders connecting the bound atoms. In contrast to the bulk case, all the Ni–Ni bond CP have disappeared, and trigonal prism-like cages (white spheres) and 5-faced cages (pink spheres) define the specific bonding polyhedral, the packing of which gives rise to the exposed structure of this surface. The topology of these polyhedra is determined only by the numbers of vertexes, edges, and faces. Vertexes are the nuclei, edges are the bond paths between nucleus and bond critical points, and each face is defined by a ring critical points. A convenient notation for them<sup>35</sup> is (vertexes number, edge number, face number). The outermost white cages describe {5, 6, 3} polyhedra (Figure 7c) with three nonplanar curved faces. Thus, the network of bond paths describing the atomic connectivity shows that the graph of the exposed structure for the 111\_S2 surface results from the packing of these {5, 6, 3} polyhedra and {10, 13, 5} polyhedra (Figure 7d) with a pink cage at the middle.

Similar to the bulk case,<sup>91</sup> the outermost Ni atoms (blue spheres in Figure 7) are 4-coordinated, linked to two three-coordinated S atoms, one on the first sulfur layer (red spheres) and one on the second (green spheres) and linked to two internal six-coordinated S atoms.  $\rho_b$  gives an indication of the amount of density accumulated in the bonding region and gives a suggestion about the strength and nature of the chemical bond.<sup>31,37–40</sup> Typical  $\rho_b$  values<sup>31</sup> for covalent bonds are 0.722, 0.551, and 0.252 au for N<sub>2</sub>, O<sub>2</sub>, and H<sub>3</sub>C–CH<sub>3</sub> bond in ethane molecules, respectively. When  $\rho_b$  is large and the charges on the atoms are small or zero as in the previous cases or SCl<sub>2</sub> ( $\rho_b$  = 0.133,  $Q_{Cl}$  = -0.20),<sup>31,40</sup> bond density accumulation within the bonding region is the major cause of the attraction between the atoms. In contrast, when  $\rho_b$  is small and the charges are large, as in LiCl ( $\rho_b$  = 0.046), NaCl ( $\rho_b$  = 0.036,  $Q_{Cl}$  = -0.87), MgCl<sub>2</sub> ( $\rho_b$  = 0.057,  $Q_{Cl}$  = -0.83), or MgO crystal<sup>93</sup> ( $\rho_b$  = 0.035), the bonds are predominately ionic.<sup>31,40</sup> When  $\rho_b$  is quite large and the atomic charges are also large, as in SiCl<sub>4</sub> ( $\rho_b$  = 0.106,  $Q_{Cl}$  = -0.69) or PCl<sub>3</sub> ( $\rho_b$  = 0.120,  $Q_{Cl}$  = -0.43), the bonds have a large covalent character and a considerable ionic character: the accumulated density in the bonding region and the atomic charges both make a substantial contribution to the attraction between the atoms.<sup>31,40</sup> These intermediate interactions are characteristic of a strongly polar bond.

The Ni–S bonds of the (111\_S2) surface possess values typical of polar covalent bonds such as that observed in pyrite-type transition metal sulfide bulk (RuS<sub>2</sub>, OsS<sub>2</sub>, IrS<sub>2</sub>, FeS, and NiS<sub>2</sub>).<sup>19</sup> For this type of material, the metal–S bonds correspond to the interaction of a relatively hard core of density on the metal with a softer, more polarizable region of electron density on S. Table 1 also shows that  $\rho_b$  systematically decreases as the Ni–S bond belongs to innermost layers.  $\rho_b$  of the outermost Ni–S bond has a value similar to RuS<sub>2</sub> (0.090 au), OsS<sub>2</sub> (0.099 au), and IrS<sub>2</sub> (0.096 au) bulk.<sup>19</sup> However, it is larger than that in the  $Ni_3S_2$  bulk case,<sup>94</sup> where  $\rho_b$  has a value of 0.076 au (as seen in Table 1).  $\rho_b$  for the bonds between the outermost Ni atoms with atoms on the third and fourth S layer is systematically smaller than the corresponding value for the  $Ni_3S_2$  bulk. For this bulk, each S atom is coordinated to six Ni atoms, and therefore there is an electronic transfer of 0.112e ( $Q_s/6$ ) by the Ni atom. The S atoms at the first and second sulfur layers are coordinated only to three Ni atoms and the electron transfer by Ni atom increase to 0.127e and 0.148e, respectively. These results demonstrate an increase, with respect to the bulk, of the outermost Ni–S bond strength at the surface. This increase is a consequence of a bigger accumulation of electronic density at the bond critical point region and an increase in the electronic transfer toward the S atoms. Both factors make an important contribution to the atomic attraction within the bonding regions.

Figure 8 shows the obtained outermost critical points for the (111̄\_S2) surface. Seven-faced (pink spheres) and five-faced (orange spheres) cages define {11, 16, 7} and {9, 12, 5} bonding polyhedra, whose packing forms the exposed atomic structure of this surface. Similar to the 111\_S2, it can be observed the presence of {5, 6, 3} trigonal polyhedra (white spheres). However, for the (111̄\_S2) case, these polyhedra are deeper than those defined by the pink and orange cages CPs. The outermost polyhedra correspond to the (11, 16, 7) type (Figure 8c) and expose a two-coordinated (red sphere) S atom. This polyhedron is defined by two outermost Ni–S bond paths, 12 internal Ni–S bonds, and two Ni–Ni bonds with  $\rho_b$  values of 0.102, 0.080, and 0.040 au, respectively, and contains a cage CP with a  $\rho_c$  value of 0.006 au. The outermost {5, 6, 3} polyhedra of the (111̄\_S2) surface (Figure 7c) are defined by six Ni–S bond paths, three external and three internal with  $\rho_b$  values of 0.091 and 0.085 au, respectively, and contain a cage CP with a  $\rho_c$  value of 0.033 au. Additionally, the (11, 16, 7) polyhedra with a cage–outermost S atom distance of 3.437 Å are less compact than the {5, 6, 3} ones of the (111\_S2) surface, which cage–outermost S atom distance of 1.718 Å. Therefore, the last

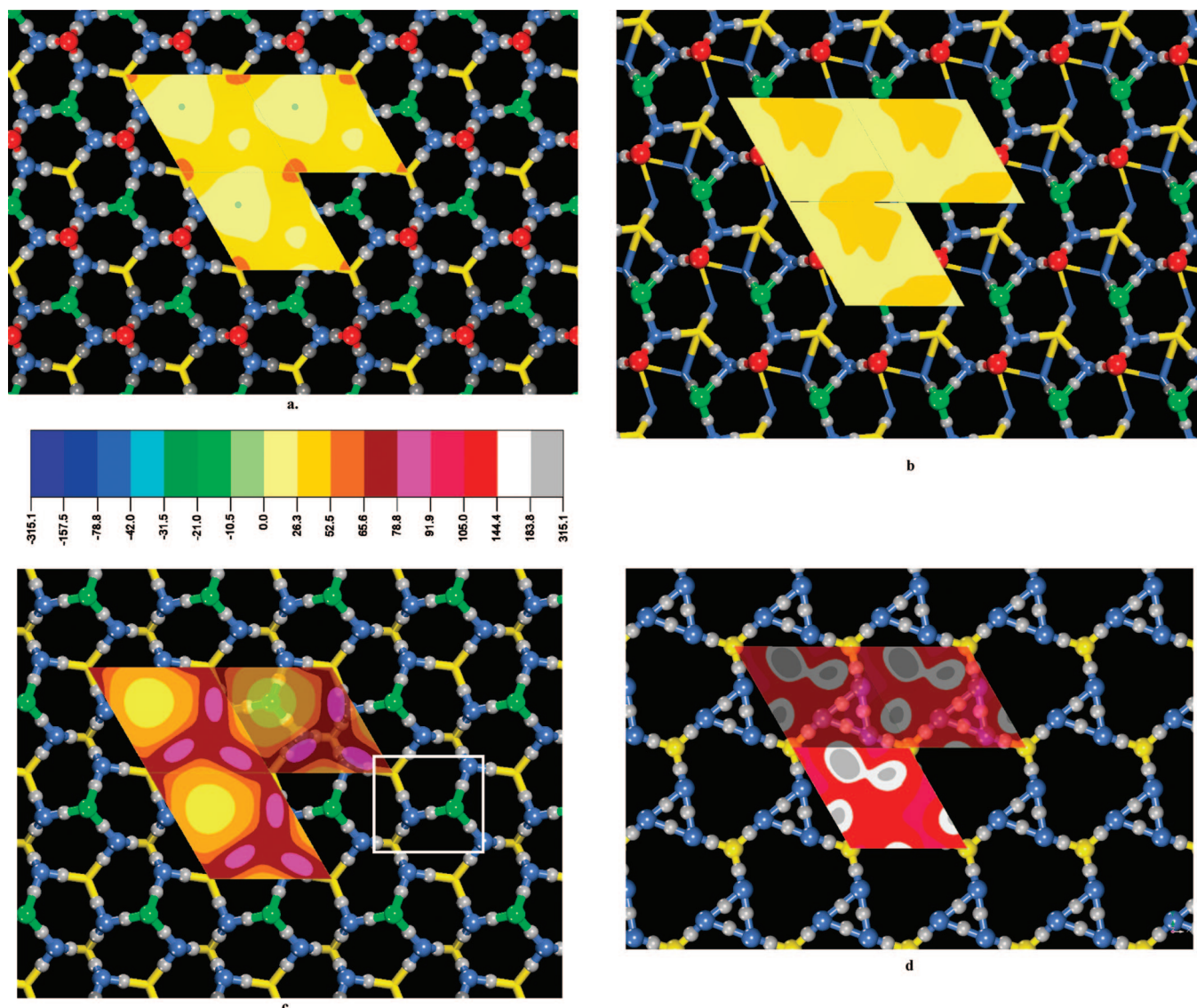


**Figure 9.** Top view of the  $V(\mathbf{r})$  mapping on the 0.001 au contour of  $\rho(\mathbf{r})$  defining the outermost border of the Ni<sub>3</sub>S<sub>2</sub> surfaces: (a) (111\_S2), (b) (111̄\_S2), (c) (111\_S1), and (d) (111̄\_S0). Blue, red, green, and small gray spheres denote the Ni, outermost and second sulfur atoms, and Ni–S bond critical points, respectively. In (c) and (d) some transparency degree for certain unit cells is applied. The tab at the bottom is blue jay (−157.530 to −78.765 kJ/mol), blue heaven (−78.765 to 42.008 kJ/mol), light blue (−42.008 to −31.506 kJ/mol), dark green (−31.506 to −21.004 kJ/mol), green (−21.004 to −10.502 kJ/mol), light green (−10.502 to 0.000 kJ/mol), light yellow (0.000 to 26.255 kJ/mol), yellow cream (26.255 to 52.510 kJ/mol), orange (52.510 to 65.638 kJ/mol), brown (65.638 to 78.765 kJ/mol), purple (78.765 to 91.893 kJ/mol), light red (91.893 to 105.020 kJ/mol), red (105.020 to 144.403 kJ/mol), white (144.403 to 183.75 kJ/mol), and gray (183.75 to 236.295 kJ/mol).

**TABLE 2: Local Maximum Positive Value of  $V(r)$  for the Studied Sites on the Nickel Sulfide Surfaces**

surface	$V_{\max}$ (kJ/mol)
(111_S2)	52.51
(111_S1)	86.64
(111_S0)	267.80
(111̄_S2)	36.76

polyhedra, whose external S atoms are bonded by a much larger electron density and also have larger atomic charges (as seen in Table 1), should be more stable than the (11, 16, 7) polyhedra of the (111̄\_S2) surface.

This conclusion agrees with the energy  $\gamma$  vs gas mixture pressure ratio variation results plotted in Figure 5. For example, at  $p_{\text{H}_2\text{S}}/p_{\text{H}_2} = 0.05$ , the energy needed to create the (111\_S1) termination from the (111\_S2) by removal of the outermost S atom (e.g., reduction energy) is around 4 times larger than that corresponding to formation of the (111̄\_S1) termination from

the (111̄\_S2) surface. The structure stability is determined thus by stable critical points, which retain their properties, and hence the shape of the charge density remains unchanged upon nuclei displacements. A structure that contains only stable critical points will thus persist over some range of all possible nuclear motions and is, therefore, a stable structure. When two or more stable critical points coalesce, however, the properties of the resulting critical points are unstable with respect to nuclear motions, as is the structure it defines. In a stable ring structure, the ring critical point is usually close to the center of the ring and far from the bond critical points. When a bond of the ring structure is extended, the resulting change in  $\rho(\mathbf{r})$  causes the ring critical point to migrate toward the bond. In an unstable ring structure, the ring critical point is very near to a bond critical point. The values of  $\rho(\mathbf{r})$  at these two critical points are nearly equal, and the negative curvature of the bond in the direction of the ring CP is much smaller in magnitude than the other negative curvature. In this sense, the ring structures of the {5,

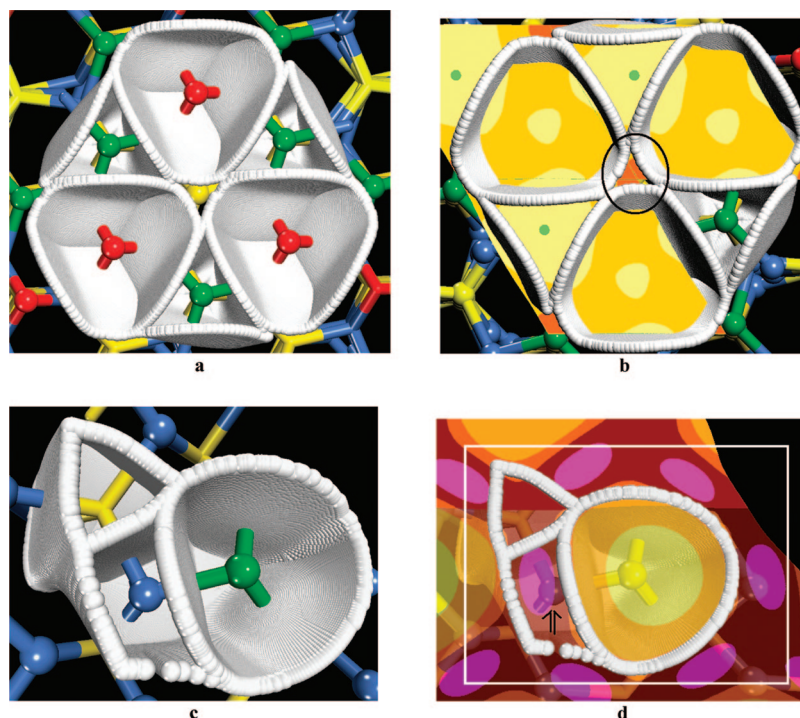


**Figure 10.** (a) Top view of the atomic basins defined by the nickel–sulfur IAS (white structures) for six outermost S surface atoms of the (111\_S2) surface. (b) Superposition of the color map on the border of the surface atoms. It can be seen that the outermost Ni atoms are almost covered by the S atoms and just a small hole (highlighted by a black circle) let access to this Ni atoms (the Lewis sites). (c) Top view of the atomic basins defined by the nickel–sulfur IAS for one Ni and two outermost sulfur atoms of the (111\_S1) surface. A purple zone (the most Lewis acidic sites) above the Ni basin can be observed. The color tab is the same as in Figure 9.

6, 3} polyhedra for the (111\_S2) surface termination are stable, while the rings of the {11, 16, 7} polyhedra for the (111\_S2) surface containing Ni–Ni bonds are unstable. For this last polyhedron, Figure 8c shows the proximity of the ring (dark blue small sphere) and the Ni–Ni bond CPs. The calculated curvatures for these Ni–Ni bond critical points are  $\lambda_1 = -0.0282$  au,  $\lambda_2 = -0.0064$  au,  $\lambda_3 = 0.1174$  au, and  $\rho_b = 0.0428$ , while the curvatures of the ring CP close to the Ni–Ni bonds are  $\lambda_1 = -0.0292$  au,  $\lambda_2 = -0.0089$  au,  $\lambda_3 = 0.10513$  au, and  $\rho_b = 0.0427$ . For both CP,  $\lambda_2$  is by far smaller than  $\lambda_1$ , and  $\rho_b$  has practically the same value. These results suggest that the origin of the larger stability of the 111\_S2 surface termination of  $\text{Ni}_3\text{S}_2$  lies in the existence of the very stable external {5, 6, 3} polyhedra.

**Electrostatic Potential Study.** Exposed surface atoms, such as an atom in an isolated molecule, have considerable open parts that extend to infinity. These atoms are open or unbounded at the exterior of the surface and a practical definition<sup>20,31,39,95</sup> is to cap the atom with an isosurface of the electron density with small  $\rho(\mathbf{r})$  value representing the van der Waals envelope of the system. This latter isosurface (usually  $\rho(\mathbf{r}) = 0.001$  au) can be considered as the practical outer limit of the atoms in molecules, crystals, or surfaces because, in general, it encompasses at least 95% of the electronic charge of the system.<sup>31</sup> HDS susceptibility of the sites on the exposed atoms can be particularly explored mapping the electrostatic potential on the  $\rho(\mathbf{r})$  isosurface capping them.<sup>20,95</sup> This mapping allows us to identify the host sites in which nucleophiles (most positive zone) and electrophiles (most negative zone) should bind. Additionally, the local maximum value of  $V(\mathbf{r})$  at the determined host zones provides a quantitative determination of the Lewis acidity strength on the outermost atoms. A top view of the  $V(\mathbf{r})$  color maps for the (111\_S2) surface model is shown in Figure 9a, while the calculated local  $V_{\max}$  value is collected in Table 2.

Starting from the most negative  $V(\mathbf{r})$  values (see caption of Figure 9), three kinds of blue and three kinds of green denote the most negative ones while two kinds of yellow, one orange, one brown, one purple, and two kinds of red denote the positive  $V(\mathbf{r})$  values. The map exhibits small areas of orange zones localized at the center of each three outermost Ni atoms, just at small holes in the basins of the outermost S atoms (see Figure 10a,b). These orange regions correspond to the most positive site and therefore to the most Lewis acidic sites. At each orange zone a  $V(\mathbf{r})$  local maximum with a value of 52.51 kJ/mol was found.

Figure 9b shows the  $V(\mathbf{r})$  color map for the (111\_S2) surface. According to our morphology study, this is the other surface orientation that might be exposed in  $\text{Ni}_3\text{S}_2$  nanoparticles. The map only exhibits yellow zones with a local maximum of 36.76 kJ/mol. Therefore, its Lewis acidic strength is smaller than that of the (111\_S2) surface termination, suggesting that the (111\_S2) surface is even less active toward HDS catalysis than the (111\_S2) one. This finding suggests that the above surfaces are weaker Lewis acids than the NiMoS edges<sup>95</sup> models with 100% ( $V_{\max} = 81.39$  kJ/mol), 33% ( $V_{\max} = 79.82$  kJ/mol), and 66% (66.69 kJ/mol) of Mo atoms substituted by Ni atoms. Additionally, the present  $\text{Ni}_3\text{S}_2$  surfaces would show a much smaller Lewis acidity as compared to the strong Lewis acidity of Mo sites on the NiMoS edge ( $V_{\max} = 210.30$  kJ/mol), at which just one outermost S atom has been removed.<sup>95</sup> These results agree with the well-known poor HDS activity of large  $\text{Ni}_3\text{S}_2$  particles supported on  $\text{Al}_2\text{O}_3$ ,  $\text{SiO}_2$ , or C with respect to the NiMoS ones.<sup>4</sup>

Figure 9c shows the corresponding  $V(\mathbf{r})$  map for the (111\_S1) case, while plots of the atomic basin for just the three nonequivalent outermost Ni and S atoms and the superposition of the  $V(\mathbf{r})$  map on those atomic basins are shown in parts c and d of Figure 10, respectively. It should be noted that sulfur

removal lets free access to the outermost Ni atoms. A purple region with a local maximum of 86.64 kJ/mol located above each Ni atom suggests a considerable increase in Lewis acidity with respect to the (111\_S2) surface and a similar acidity of exposed Ni atoms on the NiMoS edges.<sup>95</sup> Figure 9d shows a top view of the V(r) color map for the 111\_S0 surface. This map starts from red (with a minimum value of 94.52 kJ/mol), suggesting that this surface completely shows a Lewis acid character. Gray zones localized at distorted hexagonal big holes defined by each of the three nickel rings correspond to sites with the strongest Lewis acidity. These zones contain a local maximum with a value of 320.21 kJ/mol and two local maximum with a value of 202.16 kJ/mol. Thus, the (111\_S0) surface termination would show a stronger Lewis acid than the NiMoS edges, at which just one outermost S atom per Mo site was removed. Nevertheless, the (111\_S0) surface termination is the least stable (see Figure 5) of the studied Ni<sub>3</sub>S<sub>2</sub> surfaces. Therefore, sulfur atoms might be easily adsorbed at its local maxima of V(r) regenerating the (111\_S1) and (111\_S2) surface terminations. The obtained Lewis acidity behavior of the studied Ni<sub>3</sub>S<sub>2</sub> surfaces is a further manifestation of the Sabatier's principle, an intermediate Lewis acidity strength correspond to an optimal catalyst. A very high Lewis acidity as in the 111\_S0 surface makes a large attraction toward the sulfur atoms, poisoning the surface and producing a nonactive catalysts, while a low Lewis acidity as in the (111\_S2) or (111\_S2) surface termination does not attract the S atoms contained in the polluting molecules.

In summary, the present results suggests that the origin of the low HDS reactivity of Ni<sub>3</sub>S<sub>2</sub> catalysts is strongly related to the fact that the surfaces exposed by catalyst particles are completely covered with very weak Lewis acid sites. These findings contrast to those in NiMoS<sup>28,95</sup> and Ni<sub>2</sub>P cases,<sup>96,97</sup> whose most stable surface exhibit available metal sites. More factors such as support and particle size effects, hydrogen adsorbed in the form of S—H and M—H groups, formation of carbides, NiS<sub>x</sub>C<sub>y</sub> species, etc., must be considered. We are currently exploring such factors in our laboratory.

## Concluding Remarks

First-principles surface thermodynamics and morphologic studies suggests that nonsupported Ni<sub>3</sub>S<sub>2</sub> nanoparticles would expose just the (111) and (111) surface faces in HDS conditions of temperature and ratio of the gas mixture partial pressures. Extremely low Lewis acidity of these surface faces was suggested by the nature of the electrostatic potential projected at the electronic density contour corresponding to a  $\rho(\mathbf{r})$  value of 0.001 au. Consequently, the S atoms contained in the polluting molecules are practically not attracted by the surface sites exposed by Ni<sub>3</sub>S<sub>2</sub> surface cuts. Therefore, Ni<sub>3</sub>S<sub>2</sub> nanoparticles are expected to be practically inactive toward HDS catalysis.

**Acknowledgment.** This work was supported by the grant G-2000001512 from the CONICIT (Consejo Nacional de Investigaciones Científicas y tecnológicas) of Venezuela.

## References and Notes

- (1) (a) Weisser, O.; Landa, S. *Sulfide Catalysts: Their Properties and Applications*; Pergamon: Oxford, 1973. (b) Hinnemann, B.; Moses, P. G.; Norskov, J. K. *J. Phys.: Condens. Matter* **2008**, *20*, 064236.
- (2) Topsoe, H.; Clausen, B. S.; Massoth, F. *Hydrotreating Catalysis in Catalysis, Science and Technology*; Springer-Verlag: Berlin, 1996; Vol. 11.
- (3) Rodriguez, J. A.; Drovak, J.; Capitano, A. T.; Gabelnick, A. M.; Gland, J. L. *Surf. Sci.* **1999**, *429*, L462.
- (4) Pecoraro, T. A.; Chianelli, R. R. *J. Catal.* **1981**, *67*, 430.
- (5) Chianelli, R. R.; Daage, M.; Ledoux, M. *J. Adv. Catal.* **1994**, *40*, 117.
- (6) Harris, S.; Chianelli, R. R. *J. Catal.* **1984**, *86*, 400.
- (7) Topsoe, H. *Bull. Soc. Chim. Belg.* **1995**, *104*, 283.
- (8) Norskov, J. K.; Clausen, B. S.; Topsoe, H. *Catal. Lett.* **1992**, *1*, 13.
- (9) Chianelli, R. R.; Berhault, G.; Raybaud, P.; Kasztelan, S.; Hafner, J.; Toulhoat, H. *Appl. Catal., A* **2002**, *227*, 83.
- (10) Chianelli, R. R.; Daage, M.; Ledoux, M. *J. Adv. Catal.* **1994**, *40*, 117.
- (11) (a) Harris, S.; Chianelli, R. R. *J. Catal.* **1984**, *86*, 400. (b) Toulhoat, H.; Raybaud, P. *J. Catal.* **2003**, *216*, 63.
- (12) Vissers, J. P. R.; Groot, C. K.; Vanoers, E. M.; de Beer, V. H. J. *Bull. Soc. Chim. Belg.* **1984**, *93*, 813.
- (13) Ledoux, M. J.; Michaux, O.; Agostini, G.; Panisso, P. *J. Catal.* **1986**, *102*, 275.
- (14) Burdett, J. K.; Chung, J. T. *Surf. Sci. Lett.* **1990**, *236*, L353.
- (15) Smith, T. S.; Johnson, K. H. *Catal. Lett.* **1994**, *28*, 361.
- (16) Raybaud, P.; Kresse, G.; Hafner, J.; Toulhoat, H. *J. Phys.: Condens. Matter* **1997**, *9*, 11085.
- (17) Raybaud, P.; Hafner, J.; Kresse, G.; Kasztelan, S.; Toulhoat, H. *J. Catal.* **2000**, *190*, 128.
- (18) Neurock, M.; van Santen, R. A. *J. Am. Chem. Soc.* **1994**, *116*, 4427.
- (19) Aray, Y.; Rodríguez, J.; Vega, D.; Rodriguez-Arias, E. N. *Angew. Chem., Int. Ed.* **2000**, *39*, 3810.
- (20) Aray, Y.; Rodríguez, J. *J. Mol. Catal. A: Chem.* **2007**, *265*, 32.
- (21) Raybaud, P.; Hafner, J.; Kresse, G.; SKasztelan, S.; Toulhoat, H. *J. Catal.* **2000**, *189*, 129.
- (22) Clausen, B. S.; Lengeler, B.; Candia, R.; Als-Nielsen, J.; Topsoe, H. *Bull. Soc. Chim. Belg.* **1981**, *90*, 1249.
- (23) Parham, T. G.; Merrill, R. P. *J. Catal.* **1984**, *85*, 295.
- (24) Tauster, S. J.; Pecoraro, T. A.; Chianelli, R. R. *J. Catal.* **1980**, *63*, 515.
- (25) Topsoe, H.; Candia, R.; Topsoe, N. Y.; Clausen, B. S. *Bull. Soc. Chim. Belg.* **1984**, *93*, 783.
- (26) (a) Lauritsen, J. V.; Bollinger, M. V.; Lægsgaard, E.; Jacobsen, K. W.; Norskov, J. K.; Clausen, B. S.; Topsøe, H.; Besenbacher, F. *J. Catal.* **2004**, *221*, 510. (b) Schweiger, H.; Raybaud, P.; Toulhoat, H. *J. Catal.* **2002**, *212*, 33. (c) Schweiger, H.; Raybaud, P.; Kresse, G.; Toulhoat, H. *J. Catal.* **2002**, *207*, 76.
- (27) Raybaud, P.; Costa, D.; Corral-Valero, M.; Arrouvel, C.; Digne, M.; Sautet, P.; Toulhoat, H. *J. Phys.: Condens. Matter* **2008**, *20*, 064235.
- (28) Krebs, E.; Silvi, B.; Raybaud, P. *Catal. Today* **2008**, *130*, 160.
- (29) Costa, D.; Arrouvel, C.; Breysse, M.; Toulhoat, H.; Raybaud, P. *J. Catal.* **2007**, *246*, 325.
- (30) Arrouvel, C.; Breysse, M.; Toulhoat, H.; Raybaud, P. *J. Catal.* **2005**, *232*, 161.
- (31) (a) Bader, R. F. W. *Atoms in Molecules—A Quantum Theory*; Clarendon Press: Oxford, U.K., 1990. (b) Bader, R. F. W. *Chem. Rev.* **1991**, *91*, 893.
- (32) Bader, R. F. W. *J. Phys. Chem. A* **1998**, *102*, 7314.
- (33) Bader, R. F. W.; Popelier, P. L. A.; Keith, T. A. *Angew. Chem., Int. Ed. Engl.* **1994**, *33*, 620.
- (34) Zou, P. F.; Bader, R. F. W. *Acta Crystallogr.* **1994**, *A50*, 714.
- (35) Eberhart, M. E. *J. Can. Chem. Soc.* **1996**, *74*, 1229.
- (36) Eberhart, M. E. *Philos. Mag. A* **1996**, *73*, 47.
- (37) Aray, Y.; Rodríguez, J.; Vega, D. *J. Phys. Chem. B* **2000**, *104*, 4608.
- (38) Pendás, M. A.; Costales, A.; Lúaña, V. *Phys. Rev. B* **1997**, *55*, 4275.
- (39) Popelier, P. *Atoms in Molecules—An Introduction*; Prentice-Hall: Harlow, England, 2000.
- (40) Gillespie, R. J.; Popelier, P. L. A. *Chemical Bonding and Molecular Geometry: From Lewis to Electron Densities*; Oxford University Press: New York, 2001.
- (41) Ghermani, N. E.; Lecomte, C.; Dusausoy, Y. *Phys. Rev. B* **1996**, *53*, 4231.
- (42) Hénaff, C. L.; Hansen, N. K.; Protas, J.; Marnier, G. *Acta Crystallogr., B* **1997**, *53*, 870.
- (43) Ivanov, Y. V.; Belokoneva, E. L.; Protas, J.; Hansen, N. K.; Tirelson, V. G. *Acta Crystallogr., Sect. B* **1998**, *54*, 774.
- (44) Koritsanszky, T. S.; Coppens, P. *Chem. Rev.* **2001**, *101*, 1583.
- (45) Downs, R. T.; Gibbs, G. V.; Boisen, M. B., Jr; Rosso, K. M. *Phys. Chem. Miner.* **2002**, *29*, 369.
- (46) Abrams, Y. A.; Okamura, F. P. *Acta Crystallogr., Sect. A* **1997**, *53*, 187.
- (47) Takata, M.; Sakata, M.; Kumazawa, S.; Larsen, F. K.; Iversen, B. *Acta Crystallogr., Sect. A* **1994**, *50*, 330.
- (48) Vyboishchikov, S. F.; Masunov, A. E.; Streletsov, V. A.; Zorkii, P. M.; Tirelson, V. G. *Zh. Khim.* **1994**, *68*, 2024.

- (49) Boese, R.; Boese, A. D.; Blazer, D.; Antipin, M. Y.; Ellern, A.; Seppelt, K. *Angew. Chem., Int. Ed. Engl.* **1997**, *36*, 1489.
- (50) Boese, R.; Niederprum, N.; Blazer, D.; Maulitz, A.; Antipin, M. Y.; Mallison, P. R. *J. Phys. Chem. B* **1997**, *101*, 5794.
- (51) Munshi, P.; Guru Row, T. N. *Crystallogr. Rev.* **2006**, *11*, 199.
- (52) Mei, C. J.; Edgecombe, K. E.; Smith, V. H.; Heilingbrunner, A. *Int. J. Quantum Chem.* **1993**, *48*, 287.
- (53) Aray, Y.; Rodríguez, J.; Rivero, J. *J. Phys. Chem. A* **1997**, *101*, 6976.
- (54) Mori-Sánchez, P. Densidad electrónica y enlace químico. De la molécula al cristal. Ph.D. Thesis, Universidad de Oviedo, 2002.
- (55) Eberhart, M. E.; Clougherty, D. P.; MacLaren, J. M. *J. Am. Chem. Soc.* **1993**, *115*, 5762.
- (56) Eberhart, M. E.; Clougherty, D. P.; MacLaren, J. M. *J. Mater. Res.* **1993**, *8*, 438.
- (57) Haussermann, U.; Wengert, S.; Nesper, R. *Angew. Chem., Int. Ed. Engl.* **1994**, *33*, 2073.
- (58) Grosch, G. H.; Range, K. J. *J. Alloys Compd.* **1996**, *233*, 39.
- (59) Knecht, M.; Ebert, H.; Bensch, W. *J. Alloys Compd.* **1997**, *246*, 166.
- (60) Tirelson, V. G.; Zou, P. F.; Tang, T. H.; Bader, R. F. W. *Acta Crystallogr., Sect. A* **1995**, *51*, 143.
- (61) Gatti, C.; Saunders, V. R.; Roetti, C. *J. Chem. Phys.* **1994**, *101*, 10686.
- (62) Plats, J. A.; Howard, S. T. *J. Chem. Phys.* **1996**, *105*, 4668.
- (63) Luaña, V.; Costales, A.; Mori-Sánchez, P.; Pendás, M. A. *J. Phys. Chem. B* **2003**, *107*, 4912.
- (64) Blanco, M. A.; Costales, A.; Pendás, A. M.; Luaña, V. *Phys. Rev. B* **2000**, *62*, 12028.
- (65) Pendás, A. M.; Costales, A.; Luaña, V. *Phys. Rev. B* **1997**, *55*, 4285.
- (66) Reuter, K.; Stampfl, C.; Scheffler, M. *Handbook of Materials Modeling—Ab Initio Thermodynamics and Statistical Mechanics of Surface Properties and Functions*; Springer: Berlin, 2005; Vol. 1.
- (67) Cristol, S.; Paul, J. F.; Payen, E.; Bougeard, D.; Clemendot, S.; Hutschka, F. *J. Phys. Chem. B* **2000**, *104*, 11220.
- (68) Raybaud, P. *Appl. Catal., A* **2007**, *322*, 76.
- (69) Leboeuf, M.; Koster, M.; Jug, K.; Salahub, D. R. *J. Chem. Phys.* **1999**, *111*, 4893.
- (70) Gadre, S. R.; Shirsat, R. N. *Electrostatics of Atoms and Molecules*; Universities Press: Hyderabad, 2000.
- (71) (a) Pingale, S. S.; Gadre, S. R.; Batolotti, L. *J. J. Phys. Chem. A* **1998**, *102*, 9987. (b) Deshmukh, M. M.; Sastry, N. V.; Gadre, S. R. *J. Chem. Phys.* **2004**, *121*, 12402. (c) Joshi, K. A.; Gejji, S. P. *J. Mol. Struct.: THEOCHEM* **2005**, *724*, 87. (d) Tachikawa, H.; Iyama, T.; Kawabata, H. *J. Mol. Struct.: THEOCHEM* **2005**, *718*, 117.
- (72) (a) Pathak, R. K.; Gadre, S. R. *J. Chem. Phys.* **1990**, *93*, 1770. (b) Gadre, S. R.; Kulkarni, S. A.; Shrivastava, I. H. *J. Chem. Phys.* **1992**, *96*, 5253.
- (73) Gadre, S. R.; Pathak, R. K. *Proc.—Indian Acad. Sci. (Chem. Sci.)* **1989**, *102*, 18.
- (74) (a) Alhambra, C.; Luque, F. J.; Orozco, M. *J. Phys. Chem.* **1995**, *99*, 3084. (b) Kornelak, P.; Michalak, A.; Najbar, M. *Catal. Today* **2005**, *101*, 175. (c) Michalak, A. *Chem. Phys. Lett.* **2004**, *386*, 346.
- (75) Politzer, P.; Truhlar, D. G. *Chemical Applications of Atomic and Molecular Electrostatic Potentials*; Plenum: New York, 1982.
- (76) Murray, J. S.; Sen, K. D. *Molecular Electrostatic Potential: Concepts and Applications*; Elsevier: Amsterdam, 1996.
- (77) Orozco, M.; Luque, F. J. *Theor. Comput. Chem.* **1996**, *3*, 181.
- (78) Aray, Y.; Marquez, M.; Rodríguez, J.; Coll, S.; Simón-Manso, Y.; Gonzalez, C.; Weitz, D. A. *J. Phys. Chem. B* **2003**, *107*, 8946.
- (79) (a) Aray, Y.; Marquez, M.; Rodríguez, J.; Coll, S.; Simón-Manso, Y.; Gonzalez, C.; Weitz, D. A. *J. Phys. Chem. B* **2004**, *108*, 2418. (b) Aray, Y.; Rodríguez, J.; Coll, S.; Gonzalez, C.; Marquez, M. *J. Phys. Chem. B* **2004**, *108*, 18942.
- (80) Tal, Y.; Bader, R. F. W.; Erkku, J. *Phys. Rev. A* **1980**, *21*, 1.
- (81) Keith, T. A.; Bader, R. F. W.; Aray, Y. *Int. J. Quantum Chem.* **1996**, *57*, 183.
- (82) Sjoberg, P.; Politzer, P. *J. Phys. Chem.* **1990**, *94*, 3959.
- (83) Aray, Y.; Rodriguez, J.; Vega, D. In *The Quatum Theory of Atoms in Molecules: From DNA to Solid and Drug Design*; Matta, C. F., Boyd, R. J., Eds.; Wiley-VCH: Weinheim, 2006.
- (84) Aray, Y.; Rodríguez, J.; Coll, S.; Rodríguez-Arias, E.; Vega, D. *J. Phys. Chem. B* **2005**, *109*, 23564.
- (85) Mol3 is available as part of Material Studio. Accelrys Inc., San Diego, CA, 2002.
- (86) Delley, B. *J. Chem. Phys.* **1990**, *92*, 508; **2000**, *113*, 7756.
- (87) Perdew, J. P.; Burke, K.; Emzerhof, M. *Phys. Rev. Lett.* **1996**, *77*, 3865.
- (88) (a) Tilley, R. D.; Jefferson, D. A. *J. Phys. Chem. B* **2002**, *106*, 10895. (b) Welters, W. J. J.; Vorbeck, G.; Zandbergen, H. W.; de Beer, V. H. J.; van Santen, R. A. *J. Catal.* **1994**, *150*, 155.
- (89) Somorjai, G. A. *Introduction to Surface Chemistry and Catalysis*; Wiley-Interscience: New York, 1993.
- (90) Guernalec, N.; Geantet, P.; Raybaud, P.; Cseri, T.; Aouine, M.; Vrinat, M. *Oil Gas Sci. Technol.* **2006**, *61*, 515.
- (91) Fleet, M. E. *Am. Mineral.* **1977**, *62*, 341.
- (92) Berhault, G.; Lacroix, M.; Breysse, M.; Mauge, F.; Lavalle, J.-C.; Nie, H.; Qu, L. *J. Catal.* **1998**, *178*, 555.
- (93) Aray, Y.; Bader, R. F. W. *Surf. Sci.* **1996**, *351*, 233.
- (94) Recently (Gibss, G. V.; Downs, R. T.; Prewitt, C. T.; Rosso, K. M.; Ross, N. L.; Cox, D. F. *J. Phys. Chem. B* **2005**, *109*, 21788) a study of  $\rho(\mathbf{r})$  topology using a Gaussian basis set and DFT-LDA-VWN was reported.  $\rho_b = 0.497$  au for the Ni–S bond and  $Q_{Ni} = +0.37e$  was calculated at that work.
- (95) Aray, Y.; Rodríguez, J.; Vidal, A. B.; Coll, S. *J. Mol. Catal.*, **A** **2007**, *271*, 105.
- (96) Ping, L.; Rodriguez, J. A.; Asakura, T.; Gomes, J.; Nakamura, K. *J. Phys. Chem. B* **2005**, *109*, 4575.
- (97) Nelson, A. E.; Sun, M.; Junaid Abu, S. M. *J. Catal.* **2006**, *241*, 180.

JP8072798